

This is a revised version of the manuscript submitted for publication in JAMES. Please note that, the manuscript is currently under review and has yet to be formally accepted for publication. Subsequent versions of this manuscript may have slightly different content. If accepted, the final version of this manuscript will be available via the 'Peer-reviewed Publication DOI' link.

Wavelet-based wavenumber spectral estimate of eddy kinetic energy: Application to the North Atlantic

Takaya Uchida, COAPS (tuchida@fsu.edu)
Quentin Jamet, INRIA (quentin.jamet@inria.fr)
Andrew Poje, CUNY (andrewpoje@gmail.com)
Nico Wienders, FSU (wienders@fsu.edu)
William K. Dewar, FSU (wdewar@fsu.edu)

Wavelet-based wavenumber spectral estimate of eddy kinetic energy: Application to the North Atlantic

Takaya Uchida^{1,2}, Quentin Jamet^{2,3}, Andrew C. Poje⁴, Nico Wienders⁵ & William K. Dewar^{2,5}

¹Center for Ocean-Atmospheric Prediction Studies, Florida State University, Florida, USA

²Université Grenoble Alpes, CNRS, INRAE, IRD, Grenoble-INP, Institut des Géosciences de l'Environnement, Grenoble, France

³INRIA, ODYSSEY group, Ifremer, Plouzané, France

⁴Department of Mathematics, College of Staten Island, The City University of New York, New York, USA

⁵Department of Earth, Ocean and Atmospheric Science, Florida State University, Florida, USA

Key Points:

- Wavenumber spectra of eddies, defined as the fluctuations about an ensemble mean, are estimated for the North Atlantic basin.
- The wavenumber spectra and spectral flux of eddy kinetic energy and enstrophy are estimated using wavelet transform.
- We question the validity of quasi-geostrophic thinking for the Gulf Stream and offer a primitive equation extension.

Corresponding author: William K. Dewar, wdewar@fsu.edu

Abstract

An ensemble of eddy-rich North Atlantic simulations is analyzed, providing estimates of kinetic energy wavenumber spectra and spectral budget. A wavelet transform technique is used to estimate a localized ‘pseudo-Fourier’ spectrum, permitting comparisons to be made between spectra at different locations in a highly inhomogeneous and anisotropic environment. We find evidence of a Gulf Stream imprint on the near Gulf Stream eddy field appearing as enhanced levels of energy in the North-South direction relative to the East-West direction. Surprisingly, this signature holds into the quiescent interior. We detect forward cascades of energy and enstrophy but find no clear evidence of upscale energy cascades in the separated Gulf Stream region. The spectral slopes inferred from our analysis are significantly steeper than expected from quasi-geostrophic theory, but roughly in line with a primitive equation extension of the enstrophy inertial-range theory. Lastly, we propose that the spectral shapes are somewhat universal throughout our domain, over a broad wavenumber range. Deviations from this structure occur at high wavenumbers in locations characterized by strong surface fronts. A summary conclusion is that expectations built on quasi-geostrophy are at best only weakly supported in primitive equations.

Plain language summary

Describing the statistical characteristics of the weather system of the ocean, known as eddies, has been a long standing problem in the field of ocean science. This has been motivated by the fact that eddies contribute significantly to the global heat and carbon transport. Here, in analysing numerical simulations of the North Atlantic that partially resolve the eddies, we apply a relatively novel diagnostic framework based on wavelet functions to characterize the statistical nature of eddies in a realistic setting of the ocean. We find that the signature of the Gulf Stream imprints itself onto the eddy statistics.

1 Introduction

The ocean is ‘turbulent’, implying the presence of energetic and widespread spatial and temporal ‘eddies’ (Stammer, 1998; Stammer & Wunsch, 1999). It is now commonly accepted in ocean modeling that resolving these features, at least at the mesoscale, leads to ocean simulations of a much more realistic nature (Chassignet & Marshall, 2008; Chassignet et al., 2020; Griffies et al., 2015; Constantinou & Hogg, 2021; G. Xu et al.,

2022), which may have important implications for climate projections (Saba et al., 2016; Beech et al., 2022). This implies the eddy field is an integral part of the ocean structure, and necessary to include in some fashion if acceptable ocean models are to be constructed. The computational demands of eddy-resolving resolution have led to the search for eddy parameterizations that faithfully capture the dynamical role of eddies in the absence of their explicit presence (e.g. Redi, 1982; Gent & McWilliams, 1990; Gent, 2011; Jansen et al., 2019; Guillaumin & Zanna, 2021; Uchida, Deremble, & Popinet, 2022; Li et al., 2022, and references therein). It is essential therefore to understand the behavior of the eddy field in well-resolved models in order to ascertain the character eddy parameterizations should portray and to provide benchmarks for assessing the affects of any particular proposed parameterization. This paper attempts to serve these purposes by describing and applying a methodology that allows for spatial inhomogeneity in the mean flow to influence eddy characteristics. We analyze a recently developed ensemble of North Atlantic simulations (Jamet et al., 2019) and use two-dimensional wavelet analysis to diagnose the spectral structure.

Most available theoretical guidance on oceanic turbulence comes from quasi-geostrophic (QG) theory, where the combined conservations of energy and potential vorticity lead to predictions for specific shapes for wavenumber spectra. It is generally thought that the eddy field should display a so-called ‘ $-5/3$ ’ spectral slope as a result of an up-scale cascade of energy, and a ‘ -3 ’ slope due to a down-scale enstrophy cascade (Charney, 1971). Both predictions are based on the ideas of inertial ranges and involve a reasonable number of assumptions. Locality in spectral interactions, stationarity in time and homogeneity in space are amongst the most prominent assumptions; a thorough discussion appears in (Vallis, 2006). Numerical, observational and laboratory investigations in relevant settings tend to support the predictions (e.g. Gage & Nastrom, 1986; Yarom et al., 2013; Callies & Ferrari, 2013; Campagne et al., 2014).

The inertial-range ideas are usually adopted when venturing into the more dynamically complex settings of primitive equations and realistic ocean simulations (e.g. Y. Xu & Fu, 2011, 2012; Khatri et al., 2018; Vergara et al., 2019), although it is difficult to justify many of the assumptions. In particular, as will often be the focus of this paper, the presence of the Gulf Stream would seem to clearly violate spatial homogeneity in the field in which the eddies are viewed. In addition, and perhaps at an even more fundamental level, the mix of a coherent, large-scale mean with an incoherent, variable component

82 renders the definition of what constitutes an ‘eddy’ somewhat vague. One then questions
 83 what features should be focused on when constructing a spectrum (cf. Uchida, Jamet,
 84 et al., 2021). This problem of identifying or defining ocean eddies is a well known one,
 85 with an early reference being (Wunsch, 1981).

86 Another problem facing the quantification of the eddy field in an inhomogeneous
 87 setting is a lack of available techniques for analyzing the data. A favorite, and classical,
 88 method for studying wavenumber spectra employs Fourier transforming momentum (e.g.
 89 Capet et al., 2008; Callies & Ferrari, 2013; Rocha et al., 2016; Uchida et al., 2017, 2019;
 90 Khatri et al., 2018, 2021). The connection between this measure and kinetic energy (KE)
 91 comes from Parseval’s theorem, which equates the area integrated KE to the wavenum-
 92 ber integrated spectrum

$$93 \quad \int_{\mathbf{x}} |\mathbf{u}(\mathbf{x})|^2 d\mathbf{x} = \int_{\mathbf{k}} \hat{\mathbf{u}} \cdot \hat{\mathbf{u}}^* d\mathbf{k} \quad (1)$$

94 where $\hat{\mathbf{u}}$ is the Fourier transform of $\mathbf{u} = (u, v)$. This permits the interpretation of the
 95 spectrum in terms of a wavenumber dependent energy density. However, this same equiv-
 96 alence then implies the resultant spectra are averages over the domain involved in the
 97 analysis. While this does not represent a conceptual problem if the domain is spatially
 98 homogeneous, the relation of the result to the local spectrum in an inhomogeneous set-
 99 ting is not clear.

100 Our primary numerical tool to tackle these questions is a recently developed ed-
 101 dying ensemble of partially air-sea coupled North Atlantic simulations. These simula-
 102 tions have been used before in studies of North Atlantic energetics (Jamet et al., 2020),
 103 the Atlantic Meridional Overturning Circulation (AMOC; Jamet et al., 2019), Empir-
 104 ical Orthogonal Function (EOF) analyses of eddies (Uchida, Jamet, et al., 2021), and
 105 the Thickness-Weighted Averaged (TWA) feedback of the eddies on the residual-mean
 106 flow (Uchida, Jamet, et al., 2022; Uchida, Balwada, et al., 2023). A full description of
 107 the simulations appears in Jamet et al. (2019). For our purposes, the ensemble consists
 108 of 48 members exposed to *small* initial-condition uncertainties (usually referred to as *mi-*
 109 *cro* initial conditions; Stainforth et al., 2007) run at an ‘eddy-rich’ $1/12^\circ$ resolution. A
 110 map of the surface eddy Ertel’s potential vorticity (PV) appears in Fig. 1, displaying the
 111 expected activity around the Gulf Stream region, with a separation from the coastal U.S.
 112 around Cape Hatteras, and North Atlantic Current. Also shown are six marked locations
 113 which will be referred to later in the text.

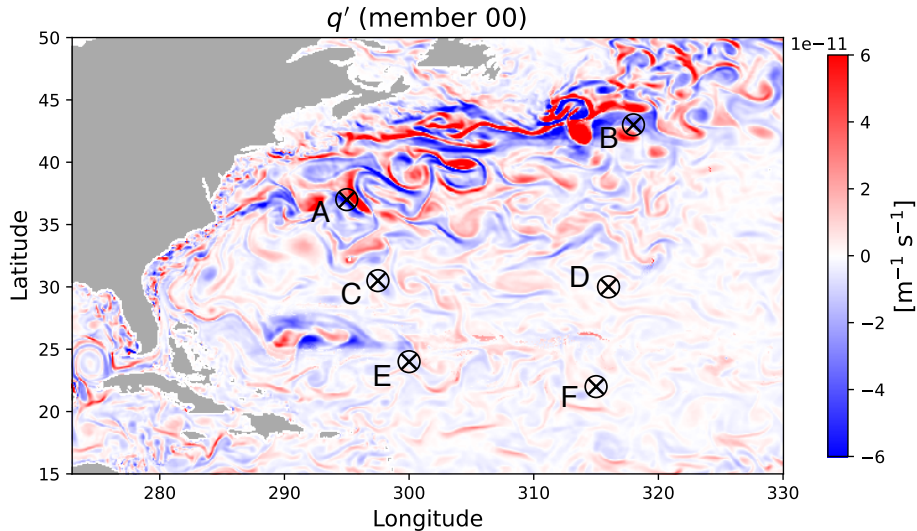


Figure 1. Surface eddy Ertel’s PV from member 00 amongst the 48 ensemble members at 00:10, January 1, 1967 where buoyancy is defined as $b = -\delta/\rho_0$ and is dimensionless (cf. Section 2.3 and Appendix A). Land and coastlines are in grey; the Gulf Stream and its extension into the open Atlantic are visible. Locations within the Gulf Stream near to separation at Cape Hatteras and North Atlantic Current are marked, as are other locations in the North Atlantic interior and gyre retroflection with six regions in total named from A to F. These will be referred to later in the text.

114 We assert that such an ensemble leads to a clear identification of oceanic eddies,
 115 namely as fluctuations about the ensemble mean. Specifically, we can average our sim-
 116 ulations at any space and time point across our ensembles to obtain an estimate of the
 117 classical ensemble mean. Then, we can revisit each individual ensemble member to com-
 118 pute its deviation from the ensemble mean at that same spatial and temporal location.
 119 Inasmuch as the ensemble mean represents that component of the solution common to
 120 all members, we identify it as the predictable part of the flow. The residuals, belonging
 121 to each individual realization, are the ‘unpredictable’ components of the flow and are iden-
 122 tified as the eddies. An attempt to rationalise this in terms of integrated KE budgets
 123 has recently been proposed by Jamet et al. (2022). Note that this eddy definition is in-
 124 dependent of any arbitrarily chosen spatial or temporal scale, a highly desirable feature
 125 not characteristic of most definitions reliant on some form of spatial or temporal filter-
 126 ing (Chen & Flierl, 2015; Uchida, Deremble, Dewar, & Penduff, 2021; Uchida, Jamet,
 127 et al., 2021). These eddies are the ones we propose to quantify.

128 As to spectral computations, we proceed using a wavelet-based analysis. To our
 129 knowledge, the wavelet approach to wavenumber spectra was initially examined by Daubechies
 130 (1992) and Perrier et al. (1995) and in an oceanographic context by Uchida, Jamet, et
 131 al. (2023). For our purposes, we will interpret the spectra computed using wavelets as
 132 an estimate of a localized ‘pseudo-Fourier’ spectrum. The locality of these estimates per-
 133 mits us to examine and compare the variability of the spectra throughout the domain.

134 Our eddy definition is reviewed briefly in the next section, along with a descrip-
 135 tion of our wavelet-based analysis methods and a possible extensions of the quasi-geostrophic
 136 (QG) inertial range theory to primitive equation. Section 3 presents a comparison be-
 137 tween wavelet-based spectral estimates and the canonical Fourier-based estimates within
 138 the North Atlantic gyre. The paper ends with a Discussion, speculations on the relevant
 139 dynamics and plans for further work.

140 **2 Theory and techniques**

141 In this section, we describe our definition of ‘eddies’ (Section 2.1) and provide an
 142 overview on wavelet analysis (Section 2.2). We also discuss possible extensions of the quasi-
 143 geostrophic (QG) inertial range theory to primitive equation in Section 2.3.

144 **2.1 Eddy Definition**

145 Due to the chaotic nature of the ocean (Poincaré, 1890; Lorenz, 1963), trajecto-
 146 ries of eddying numerical simulations are sensitive to initial condition uncertainties (Sérazin
 147 et al., 2017; Leroux et al., 2018; Jamet et al., 2019; Zhao et al., 2021; Uchida, Derem-
 148 ble, & Penduff, 2021). This allows us to develop an ensemble of ocean simulations, dif-
 149 fering only in small ways in their initial conditions; i.e. simulations based on initial states
 150 that have small differences well within current measurement uncertainties. It is a mat-
 151 ter of experience that while gross characteristics of the resulting fully evolved states are
 152 similar (there will always be a Gulf Stream, for example), the mesoscale fields become
 153 incoherent. While each ensemble solution represents an equally valid and plausible sim-
 154 ulation of the North Atlantic, none of them at any specified date will recreate the ob-
 155 served ocean state since the observed ocean is itself a single realization of the chaotic sys-
 156 tem.

From such an ensemble, one can take an ‘ensemble mean’, which we will denote by brackets, i.e. for any model variable $\psi(\mathbf{x}, t)$,

$$\langle \psi(\mathbf{x}, t) \rangle = \frac{1}{N} \sum_{i=1}^N \psi^i(\mathbf{x}, t), \quad (2)$$

where N is the total number of ensemble members and the superscript i denotes the ensemble member. We interpret the ensemble mean as the ‘forced’ response of the ocean. That is, as the ensemble mean is common to all members, it reflects the common external conditions imposed at the boundaries of the system. In our case, these common conditions consist of the prescribed atmospheric states and the open ocean boundary conditions at the northern and southern domain boundaries and the Strait of Gibraltar (Jamet et al., 2019).

The eddy field is denoted by deviations of ψ about the ensemble mean

$$\psi'^i(\mathbf{x}, t) = \psi^i(\mathbf{x}, t) - \langle \psi(\mathbf{x}, t) \rangle. \quad (3)$$

Each member, i , having its own eddy field thus identifies the eddies as an unpredictable component of the flow. Note that the ensemble mean in (2) is inherently a function of space and time, a feature which permits the examination of the non-stationary and inhomogeneous character of the statistics. It is a strength of the ensemble approach that these features of the statistics are preserved.

Finally, we note that the ensemble mean structure of the ocean is not independent of the eddies, rather the equations of motion in their non-linearity involve higher-order measures of the eddies as part of their balance. Each realization, in turn, is constrained by the lower-order statistics of the eddy contributions.

2.2 Spectral Considerations

We depart from the classical Fourier approach to compute wavenumber spectra for our non-periodic and inhomogenous settings, but do note the utility of wavenumber spectrum emerges largely from Parseval’s equality (cf. Uchida, Jamet, et al., 2023, their Appendix A). We base our spectral analysis on wavelet decompositions. Here, we provide a brief overview.

Given a function of two spatial dimensions, $f(\mathbf{x})$, its continuous wavelet transform is given by

$$\tilde{f}(s, \phi, \gamma) = \int_{\mathbf{x}} f(\mathbf{x}) \frac{1}{s} \xi^* \left(\mathbf{R}^{-1} \cdot \left(\frac{\mathbf{x} - \gamma}{s} \right) \right) d\mathbf{x}, \quad (4)$$

187 where \mathbf{R}^{-1} is the inverse of the rotation matrix

$$188 \quad \mathbf{R}^{-1} = \begin{pmatrix} \cos(\phi) & \sin(\phi) \\ -\sin(\phi) & \cos(\phi) \end{pmatrix}, \quad (5)$$

189 for rotation through an angle ϕ . The quantity s is referred to as the ‘scale’, $\boldsymbol{\gamma} (\in \mathbf{R}^2)$
 190 is the two-dimensional coordinates of interest, $\xi(\mathbf{x})$ is the so-called ‘mother’ wavelet and
 191 $\xi(\mathbf{R}^{-1} \cdot (\mathbf{x} - \boldsymbol{\gamma}) / s)$ in (4) are the daughter wavelets. The quantities \tilde{f} are the wavelet
 192 coefficients. Subject to a few, relatively easy to meet conditions (Uchida, Jamet, et al.,
 193 2023), the original data can be reconstructed from the wavelet coefficients via an inverse
 194 wavelet transform

$$195 \quad f(\mathbf{x}) = \mathcal{C} \int_{\boldsymbol{\gamma}} \int_{\phi} \int_s \frac{1}{s^4} \tilde{f}(s, \phi, \boldsymbol{\gamma}) \xi(\mathbf{R}^{-1} \cdot \left(\frac{\mathbf{x} - \boldsymbol{\gamma}}{s} \right)) ds d\phi d\boldsymbol{\gamma} \quad (6)$$

196 where \mathcal{C} is a constant, to be clarified below. Exploiting the properties of wavelets, it is
 197 possible to show they satisfy a generalized Parseval’s equality

$$198 \quad \int_{\mathbf{x}} f(\mathbf{x}) g(\mathbf{x}) d\mathbf{x} = \int_{\boldsymbol{\gamma}} \int_{\phi} \int_s \frac{\tilde{f} \tilde{g}^*}{s^3} ds d\phi d\boldsymbol{\gamma}, \quad (7)$$

199 with \bullet^* the complex conjugate. Note, if $f = g$, (7) corresponds to the equality in (1).

200 We employ the so-called Morlet wavelet (Morlet et al., 1982; Gabor, 1946), i.e.

$$201 \quad \xi(\mathbf{x}) = (e^{-2\pi i \mathbf{k}_0 \cdot \mathbf{x}} - c_0) e^{-\frac{\mathbf{x} \cdot \mathbf{x}}{2x_0^2}}, \quad (8)$$

202 where c_0 is a constant included to insure that the wavelet has zero mean $\int_{\mathbf{x}} \xi(\mathbf{x}) d\mathbf{x} =$
 203 0. The central wavenumber \mathbf{k}_0 is taken to be $\mathbf{k}_0 = (k_0, 0)$ and the quantity x_0 is a ref-
 204 erence length scale, here taken to be 50 km, viz. the length scale of the mother wavelet.
 205 We will choose $k_0 = 1/x_0$, in which case the constant c_0 is quite small and generally
 206 ignored (i.e. $c_0 = 0$), a convention adopted in this paper. Plots of (8) are found in Fig. 2.
 207 Note that the Morlet mother wavelet consists of a wave of wavelength $L = x_0$ inside
 208 a Gaussian envelope of decay scale $\sqrt{2}x_0$. Thus for $s = 1$ and $\phi = 0$, the wavelet co-
 209 efficient produced by this transformation comments on the presence of the wavenumber
 210 $\mathbf{k}_0 = (k_0, 0)$ at location $\boldsymbol{\gamma}$ in the original data. Increasing the rotation angle ϕ and fil-
 211 tering returns information about the presence of the same wavelength at angle ϕ . Finally
 212 allowing s to vary modifies the filter so that the primary wavelength of the filter is $k =$
 213 $1/(sx_0)$. The Morlet wavelet coefficient can thus be thought of as a ‘local’ Fourier trans-
 214 form at wavenumber $\mathbf{k}_0^T \cdot \mathbf{R}^{-1}(\phi) / s$, where the superscript τ denotes a transpose.

215 At this point, the scale factor in (4), s , is non-dimensional. It is more traditional
 216 in oceanography to discuss energy spectra in terms of wavenumber. As pointed out above,

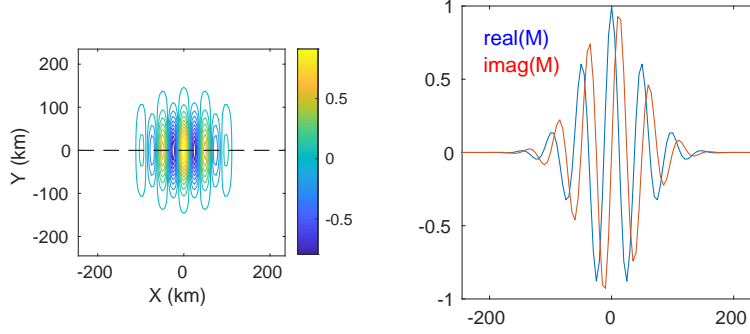


Figure 2. Structure of the Morlet wavelet. A contour plot of the real part of the mother Morlet wavelet is shown in the left panel. Transects of the real and imaginary parts along the dashed line appear in the right panel. The reference lengthscale is $x_0 = 50$ km.

217 the effective wavenumber associated with s is $k = 1/(sx_0) = 1/s_0$, where the quan-
 218 tity s_0 has units of length. Upon some algebra, one may transform (7) (with $f = g$)
 219 to wavenumber, $k = 1/s_0$, space, ending with

$$220 \int_{\mathbf{x}} f^2(\mathbf{x}) d\mathbf{x} = \frac{1}{C_{\Xi}} \int_{\phi} \int_k \int_{\gamma} \tilde{f}^* \tilde{f} k x_0^2 d\gamma dk d\phi, \quad (9)$$

221 where $C_{\Xi} = \int_{\mathbf{k}} \frac{\hat{\Xi}^* \hat{\Xi}}{\mathbf{k} \cdot \mathbf{k}} d\mathbf{k}$ and $\hat{\Xi}$ is the Fourier transform of the mother wavelet (cf. Uchida,
 222 Jamet, et al., 2023). Note, $\mathcal{C} = C_{\Xi}^{-1}$ in (7).

223 If we now produce wavelet coefficients for the zonal and meridional eddy veloci-
 224 ties u'^i and v'^i from member i of our ensemble, and manipulate them appropriately, we
 225 obtain

$$226 \tilde{E}_K^i(\gamma, \phi, k) = \frac{1}{C_{\Xi}} \frac{\tilde{u}'^i \tilde{u}'^{i*} + \tilde{v}'^i \tilde{v}'^{i*}}{2} x_0^2 k, \quad (10)$$

227 as a measure of energy density in wavelet transform space. Each value of \tilde{E}_K^i is a ran-
 228 dom number as each ensemble member possesses a ‘random’ eddy field emerging from
 229 the non-linearities in the system. Ensemble averaging those values returns an estimate
 230 of the ensemble-mean energy spectrum as a function of wavenumber k in direction ϕ . The
 231 spatial locality of the mother wavelet permits the interpretation of $\tilde{E}_K(s, \phi, \gamma) = \langle \tilde{E}_K^i(s, \phi, \gamma) \rangle$
 232 as the local energy spectrum at location γ .

233 In calculating the wavelet coefficients, we spatially interpolate each $10^\circ \times 10^\circ$ do-
 234 main centered around each \otimes in Fig. 1 onto a uniform grid (cf. section 3). The wavelet
 235 transform appropriate to the scale factor s was then taken between $[k_F^{\min}, k_F^{\max}]$ with 40

236 monotonic increments where k_F^{\min} and k_F^{\max} are the minimum and maximum Fourier wavenum-
 237 bers respectively leaving us with 47 increments, and angle ϕ with the resolution of $\pi/18$ radian (=
 238 10°) between $[0, \pi)$. The scaling was then truncated at scales below 50 km and appended
 239 with scales corresponding to the Fourier wavenumbers to increase the wavenumber res-
 240 olution at higher wavenumbers. The spatial integration of the product of the wavelet and
 241 the data is the wavelet coefficient for each location.

242 **2.3 Dimensional analysis of isotropic spectral slopes**

243 To interpret our spectral slope estimates and recast them within the inertial-range
 244 theory, we provide here a scaling for the Ertel PV by extending usual QG thinking for
 245 primitive equations. It is interesting to consider inertial range arguments in terms of \tilde{E}_K .
 246 We assume for convenience that the mother wavelet is a dimensionless function, in which
 247 case the wavelet transform \tilde{u} carries the dimensions L^3T^{-1} and C_Ξ the units L^4 . Thus,
 248 the units of \tilde{E}_K are L^3T^{-2} . A cross-scale energy flux ε must have dimensions of L^2T^{-3}
 249 and the usual inertial range arguments lead to

$$250 \quad \tilde{E}_K \propto \varepsilon^{2/3} k^{-5/3}, \quad (11)$$

251 in the energy cascade range (Vallis, 2006). In quasi geostrophy, a materially conserved
 252 quantity is QG potential vorticity (PV) and its enstrophy flux (η_{QG}) has the dimensions
 253 of T^{-3} . If we assume a so-called inertial enstrophy range, characterized by constant en-
 254 strophy flux, similar dimensional arguments yield the classical

$$255 \quad \tilde{E}_K \propto \eta_{\text{QG}}^{2/3} k^{-3}. \quad (12)$$

256 spectral shape. Accepting the usual QG idea that the enstrophy spectrum is given by
 257 $\tilde{Z}_K = k^2 \tilde{E}_K(k)$, one obtains a -1 law for the enstrophy spectra.

258 Here, we consider an extension of these ideas for primitive equations. In the richer
 259 dynamics of primitive equations, we can write a conservation equation

$$260 \quad \frac{Dq}{Dt} \approx 0, \quad (13)$$

261 for Ertel's PV $q = \boldsymbol{\omega} \cdot \nabla b = (f + \zeta) b_z + (\mathbf{k} \times \mathbf{u}_z) \cdot \nabla_{\text{h}} b$ where $\boldsymbol{\omega}$ is the absolute vorticity, b
 262 buoyancy (detailed in Appendix A), and \mathbf{k} the vertical unit vector. The horizontal gra-
 263 dents of vertical velocity are neglected consistent with the hydrostatic approximation
 264 of our simulation (Vallis, 2006).

265 From a dimensional perspective, we argue the units of b are immaterial; it is possible
 266 to write a PV equation as (13) where ‘ b ’ is replaced by any thermodynamic variable,
 267 Θ , such that

$$268 \quad \frac{D\Theta}{Dt} \approx 0, \quad (14)$$

269 so that surfaces of Θ are nearly material. In the following analysis, we take b to be dimensionless,
 270 which is equivalent to buoyancy divided by gravity. Thus, the relevant dimensions of q become $L^{-1}T^{-1}$
 271 and the enstrophy flux (η_{PE}) has dimensions $L^{-2}T^{-3}$. In an inertial range where the time scale is set by a constant PV flux,
 272 standard dimensional arguments imply that the energy spectrum should scale as
 273

$$274 \quad \tilde{E}_K \propto \eta_{PE}^{2/3} k^{-13/3}, \quad (15)$$

275 a spectral slope close to -4.3 . Due to the richer definition of Ertel’s PV compared to QGPV,
 276 a simple spectral relation between the KE and enstrophy spectrum does not exist.
 277

278 **3 Results**

279 In this section, we examine the kinetic energy (KE) and enstrophy spectra and spectral flux from the various locations in Fig. 1; the location of the panels correspond to the
 280 locations on the map. We remind the reader that enstrophy here is defined by Ertel’s potential vorticity (PV). The depth of 452 m was chosen to be within the general wind-driven
 281 circulation but beneath the mixed layer in order to avoid KE input from convective events, in our case parametrized by the K-profile parametrization (KPP; Large et al., 1994).
 282 Prior to taking the wavelet transforms, the fields were linearly interpolated onto a uniform grid. In order to account for the finite-volume discretization of MITgcm,
 283 we first weighted the velocity fields by the grid area. The velocities were then linearly interpolated onto the uniform grid and divided by the area also interpolated onto the
 284 uniform grid. The uniform grid spacings were taken as the minimum spacing per $10^\circ \times 10^\circ$ domain centered around each location in Fig. 1. The wavelet transforms are taken
 285 at the center of the $10^\circ \times 10^\circ$ domain while the Fourier transforms are taken over the $10^\circ \times 10^\circ$ domain. The 48-member ensemble outputs used in this study are instantaneous
 286 snapshots at 00:10, January 1, 1967, viz. there is no temporal averaging applied.
 287
 288
 289
 290
 291
 292
 293

294 **3.1 The wavelet and Fourier approach**

295 One of the major differences between quasi geostrophy and primitive equations is
 296 that advection is two-dimensional (2D) in the former and three-dimensional (3D) for the
 297 latter. It can be argued that for primitive equations, the eddy velocity defined about the
 298 thickness-weighted averaged residual mean, which reduces to 2D under adiabatic con-
 299 ditions (Young, 2012; Marshall et al., 2012; Aoki, 2014; Loose et al., 2022; Uchida, Bal-
 300 wada, et al., 2023), corresponds to the QG eddy velocities under order-Rossby number
 301 fluctuations in the layer thickness. Nonetheless, the spectral flux of KE and enstrophy
 302 have commonly been examined in geopotential coordinates (e.g. Capet et al., 2008; Ar-
 303 bic et al., 2013; Khatri et al., 2018, 2021; Ajayi et al., 2021). Due to the discrepancies
 304 between quasi geostrophy and primitive equations in geopotential coordinates, there is
 305 no guarantee that the inertial-range theory should hold for the latter. In this section,
 306 we examine the agreement between the wavelet and Fourier approach, and to what ex-
 307 tent the spectra and spectral fluxes in geopotential coordinates are consistent with QG
 308 predictions. We also include contributions from vertical advection unlike studies using
 309 satellite observations where only the horizontal velocities are available (Scott & Wang,
 310 2005).

311 We start by examining the wavenumber spectrum derived from the wavelet and Fourier
 312 method; the agreement between the two is impressive with the black and red curves over-
 313 lying with each other (Fig. 3a). Such a similarity between Fourier and wavelet estimates
 314 have also been identified in doubly periodic homogeneous quasi-geostrophic simulations
 315 where Fourier modes are best suited (Uchida, Jamet, et al., 2023). Prior to taking the
 316 Fourier transform, land cells surrounded by ocean were linearly interpolated over and
 317 filled in with zeros otherwise, after which a Hann window was applied to make the data
 318 doubly periodic. While neither procedure is necessary in the wavelet method, in order
 319 to make a fair comparison, we also take the wavelet transform over the fields with land
 320 cells filled in but without the windowing. The two approaches agree well in their spec-
 321 tral estimates being within the 95% bootstrap confidence interval of each other. The boot-
 322 strapping was done by randomly resampling (with replacement) the 48 ensemble mem-
 323 ber energy densities 9999 times. The overall spectral slopes are relatively steep. A best
 324 fit to the spectra between roughly 250 km and 40 km suggests a -4.13 power law, which
 325 is considerably steeper than either the -3 or $-5/3$ energy and enstrophy inertial range
 326 laws emerging from quasi geostrophy.

327 In the ocean, it is unlikely that the sources and sinks of energy are localized in wavenum-
 328 ber as assumed by standard, idealized inertial-range theories. We explicitly examine this
 329 by computing the ‘dynamics’, i.e. computing all the terms in the eddy KE spectral bud-
 330 get

$$331 \quad T_K = P_K + A_K + \text{MtE}_K + \mathcal{K}_K \quad (16)$$

332 where the tendency of KE, T_K , equals the sum of pressure work P_K , advection A_K , KE
 333 exchange with the mean flow MtE_K , and non-conservative terms \mathcal{K}_K respectively. De-
 334 tailed notations of each term are given in (B6). Our form of pressure work consists only
 335 of the wavelet transforms related to $-\langle \mathbf{u}' \cdot \nabla_{\text{h}} \phi' \rangle$. Adding and subtracting $\langle w'b' \rangle$ and
 336 using the hydrostatic relationship demonstrates that exchanges between potential and
 337 kinetic energies are contained in this term. We do not consider potential energy explic-
 338 itly here, leaving this as a topic for consideration elsewhere.

339 The relative contributions of terms in the spectral budget computed at location A
 340 are shown in Fig. 3b where the residual (grey dashed line) is seen to be negligible. Pos-
 341 itive values indicate a source for the eddy KE reservoir and negative values a sink at a
 342 given wavenumber. The largest values from the dynamics belong to pressure work, KE
 343 tendency and advection. However, all the quantities, except for advection, are not dis-
 344 tinguishable from zero at the 95% confidence level. The advection A_K is positive across
 345 all wavenumbers, which would imply a forward cascade of energy. We have examined the
 346 spatial stability of these quantities by evaluating the dynamics in the vicinity of loca-
 347 tion A, up to 70 km away. The tendencies seen in the plot hold over the area, most im-
 348 portantly the advective effects are positive and significant, consistent with a forward cas-
 349 cade.

350 We have also computed Ertel’s PV spectra at this depth (Fig. 3c). QG reasoning
 351 in a region of forward enstrophy cascade would argue for a -1 slope, which is shown by
 352 the dashed line. Clearly the spectral drop-off is much greater than this, consistent with
 353 the steep KE spectra, but shoals towards -1 at scales larger than ~ 250 km potentially
 354 indicating a QG scaling.

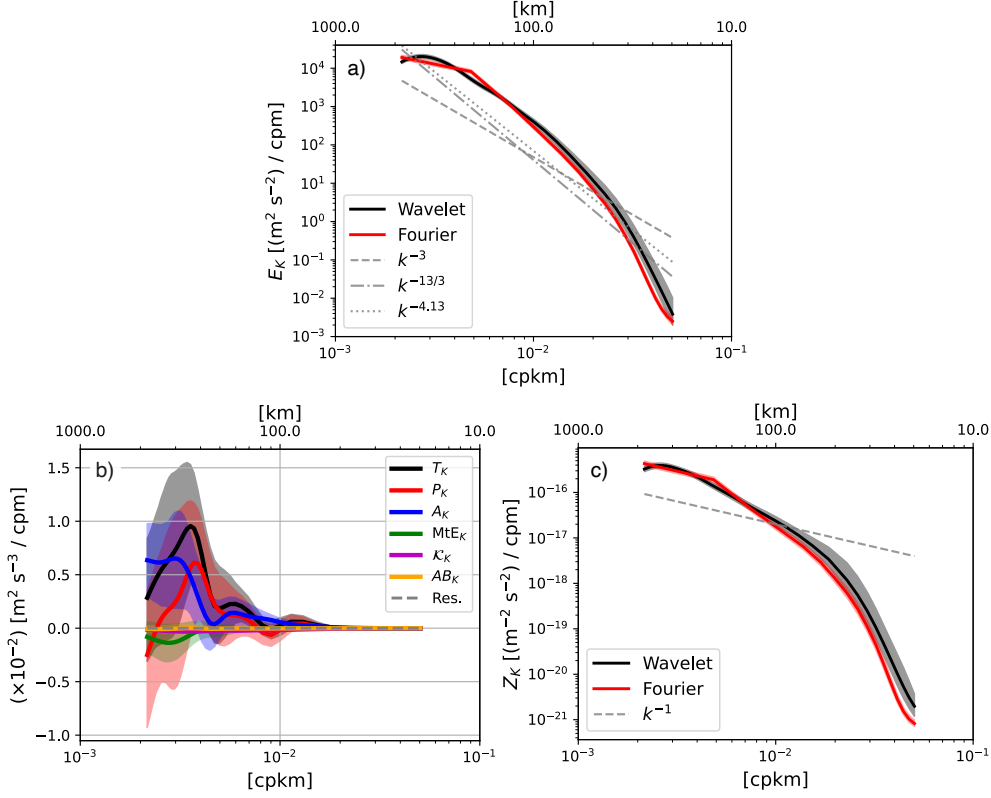


Figure 3. Isotropic (azimuthally-integrated) KE spectrum $E_K(k)$ using the wavelet and Fourier approach from $z = -452$ m at location A (indicated in Fig. 1) shown as black and red curves respectively on January 1, 1967 (a). The isotropic wavelet spectral KE budget (B6) is shown in panel (b) with the AB_K term stemming from the Adam-Bashforth time stepping. The residual in the spectral budget is shown as the grey dashed curve being negligible. The isotropic enstrophy spectrum $Z_K(k)$ where buoyancy is dimensionless (cf. Section 2.3) (c). The land cells are interpolated over except for the budget. The colored shadings indicate the 95% bootstrap confidence interval.

Using the spectral transfers, we can diagnose the KE and enstrophy spectral flux given respectively as

$$\tilde{\varepsilon}_K(\gamma, \phi, k) = -\frac{1}{C_\Xi} \int_{k > \kappa} \mathcal{R} \left[\langle \tilde{u}'^* (\mathbf{v} \cdot \nabla u)' \rangle + \langle \tilde{v}'^* (\mathbf{v} \cdot \nabla v)' \rangle + \langle \tilde{u}'^* \nabla \cdot \langle \mathbf{v}' u' \rangle \rangle + \langle \tilde{v}'^* \nabla \cdot \langle \mathbf{v}' v' \rangle \rangle \right] x_0^2 \kappa d\kappa, \quad (17)$$

$$\tilde{\eta}_K(\gamma, \phi, k) = -\frac{1}{C_\Xi} \int_{k > \kappa} \mathcal{R} \left[\langle \tilde{q}'^* (\nabla \cdot \mathbf{v} q)' \rangle + \langle \tilde{q}'^* \nabla \cdot \langle \mathbf{v}' q' \rangle \rangle \right] x_0^2 \kappa d\kappa, \quad (18)$$

where $\mathcal{R}[\cdot]$ indicates the real part (Appendix B). Positive values indicate a forward cascade towards smaller scales and negative values an inverse cascade towards larger scales.

364 The Fourier equivalent of (17) corresponds to the kinetic energy spectral fluxes often ex-
 365 amined by others. The azimuthally-integrated KE spectral flux $\tilde{\epsilon}_K$ displays a forward
 366 cascade at all scales, consistent with the Fourier-based estimate (Fig. 5a). The levels of
 367 kinetic energy exchange with the mean flow are quite low, and insignificant (green curve
 368 in Fig. 3b). The pressure work term, while noisy, tends to peak at around 250 km (red
 369 curve in Fig. 3b), so QG theory might argue for an upscale energy cascade at smaller
 370 wavenumbers (Vallis, 2006). This is not what we find, however, arguing for a deviation
 371 from quasi geostrophy in our results. We have also investigated the temporal stability
 372 of these results by looking at the following Jan. 6 and 11 outputs. The lack of signifi-
 373 cance for most of the sizeable quantities, like pressure work and kinetic energy tendency
 374 manifest in greatly different values for these quantities on those dates. Clearly, they are
 375 not stable in sign (Fig. 4). In contrast, advection is persistently positive and significant
 376 at the 95% level and scales above ~ 300 km at point A. The deviation from quasi geostro-
 377 phy in the separated Gulf Stream region is consistent with a recent study which exam-
 378 ined the energetics in the North Atlantic subtropical gyre (Jamet et al., 2020).

379 In contrast to the spectral energy flux, the isotropic spectral flux of Ertel’s enstro-
 380 phy at location A (Fig. 5b) is relatively scale independent and positive in the wavelet
 381 analysis, albeit with sizeable uncertainties. As in the KE flux, the wavelet approach shows
 382 reduced uncertainty at the largest scales where the Fourier flux is likely affected by the
 383 windowing (cf. Uchida, Jamet, et al., 2023). The presence of an extended range of scales
 384 with constant η_K , as discussed in Sec 2.3, is consistent with the observations of spectral
 385 slopes steeper than standard QG estimates.

386 Given that the wavelet technique agrees well with the Fourier method with the ad-
 387 ditional strengths of: i) negating the necessity for the data to be periodic, ii) flexibility
 388 in defining the wavenumber resolution via the scaling s , and iii) being able to extract
 389 the anisotropy in the flow through the rotational matrix \mathbf{R} , we apply our method to five
 390 other locations in the North Atlantic subtropical gyre.

391 **3.2 Wavelet spectra of the North Atlantic domain**

392 We take advantage of our wavelet approach in this section; we do not interpolate
 393 over land and take the spatial integration (4) by treating them as missing data and plot
 394 the orientations with the maximum and minimum integrated power over wavenumber,

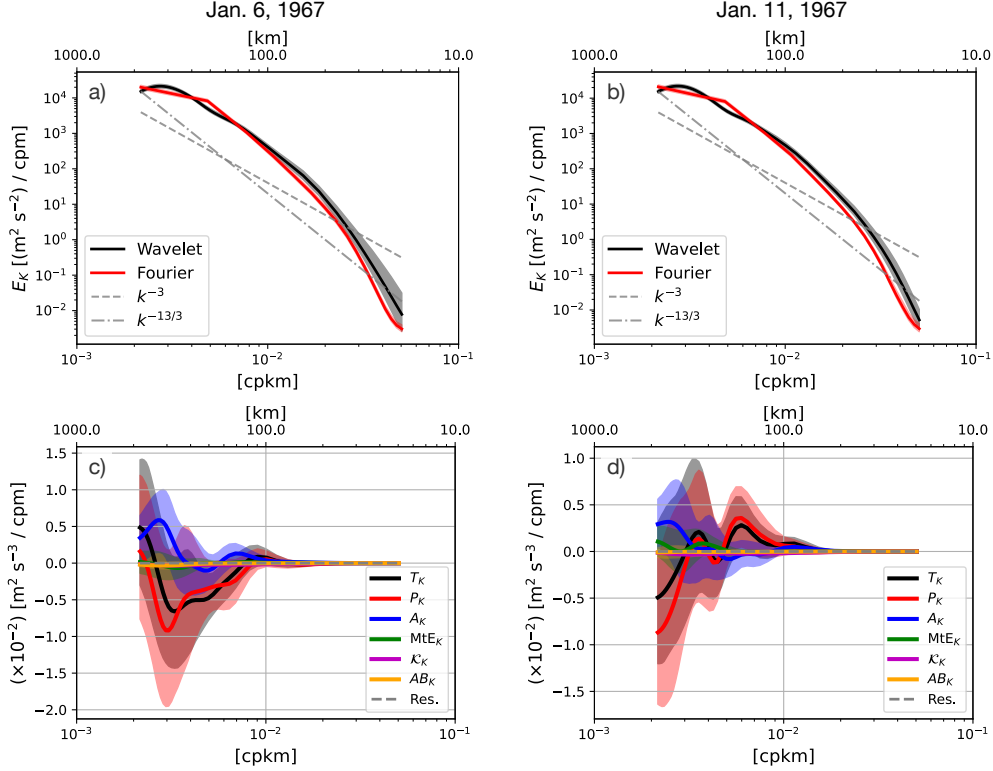


Figure 4. The KE spectra and spectral budget at location A on January 6 and 11, 1967 from $z = -452$ m. The land cells are interpolated over for the spectra to make the Fourier and wavelet approach consistent with each other but are not interpolated for the budgets.

395 i.e. energy. The maximum and minimum tend to be oriented perpendicular to one an-
 396 other (Fig. 6). We first examine a location close to the Gulf stream separation point, as
 397 seen in Fig. 1 (location A; Fig. 6a), which exhibits the highest energy levels (close to 10^3 ($\text{m}^2 \text{s}^{-2}$)/cpm)
 398 among all analysed regions. A dashed line indicating a -3 slope appears in grey; the spec-
 399 trum aligns reasonably well with this slope for a small range at the lowest wavenumbers,
 400 and then transitions to steeper decays for higher wavenumbers as already observed in
 401 Fig. 3a. The -3 slope is consistent with that expected from a forward QG enstrophy cas-
 402 cade. A statistically significant signal of anisotropy is apparent, characterized by enhanced
 403 energy in the meridional direction relative to the zonal direction. This is likely an im-
 404 print of the Gulf Stream on the eddy field due to the roughly zonal orientation of the
 405 separated Gulf Stream.

406 Moving downstream in the North Atlantic Current region (location B; Fig. 6b), the
 407 spectral slopes are similar to location A across a wide range except for the smallest wavenum-

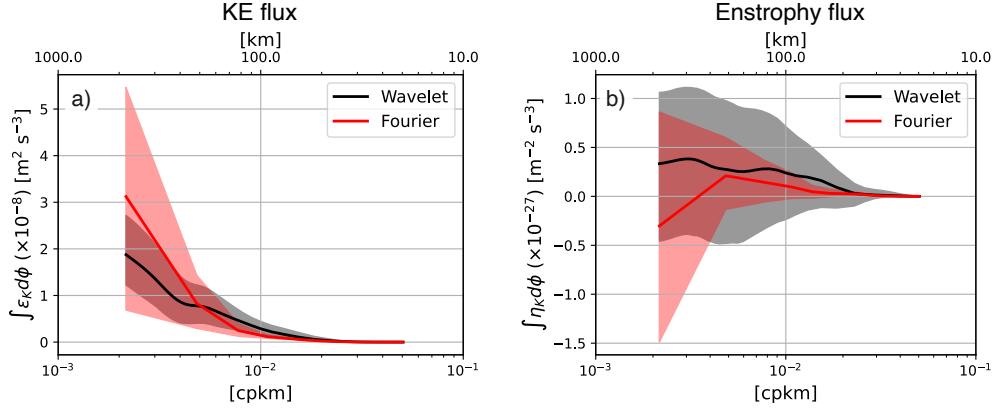


Figure 5. Isotropic (azimuthally-integrated) spectral KE flux ε_K (a), equivalent to A_K integrated in wavenumber, and spectral flux of Ertel’s enstrophy η_K at location A from $z = -452$ m on January 1, 1967 (b). The Fourier approach has the land cells interpolated over and is windowed while neither are applied for the wavelet approach. The colored shadings indicate the 95% bootstrap confidence interval.

408 bers. In stark contrast to A, no statistically significant evidence of anisotropy is seen.
 409 The spectral amplitudes have dropped from A by about a factor of three. Location C
 410 is roughly from a location on the edge of the so-called ‘inertial recirculation’ (Fig. 6c).
 411 A broad wavenumber band exhibits a steep slope, with best fit line of -4.2 , and simi-
 412 larly to B exhibits little to no evidence of anisotropy. Spectral amplitudes are compa-
 413 rable to those at B.

414 The remaining three regions (locations D-F; Fig. 6d-f) come from locations that
 415 are ostensibly in the interior of the general circulation, at locations where one might an-
 416 ticipate QG dynamics would govern. Mean flows are weak and do not exhibit much struc-
 417 ture on the deformation scale, generating conditions in which isotropy might be antic-
 418 ipated. In accord with these expectations, all three regions have the weakest energy lev-
 419 els, and all are comparable in amplitude. Beyond this, however, the results are quite sur-
 420 prising. Most unexpectedly, all three locations exhibit statistically significant anisotropy,
 421 in a sense similar to that at location A. Namely, North-South (nominally) spectra are
 422 more energetic than East-West spectra. The spectral slopes are also all steep, and simi-
 423 lar to those seen in locations A-C. This is difficult to ascribe to QG dynamics. In short,
 424 our quantitative measures of the eddy field in the ocean interior do not meet with our
 425 expectations.

426 Along with the spectra, we exhibit the eddy anisotropy angles defined as (Waterman
427 & Lilly, 2015)

$$428 \quad \vartheta = \frac{1}{2} \arctan \left(\frac{2\langle u'v' \rangle}{\langle u'^2 - v'^2 \rangle} \right). \quad (19)$$

430 The angles north of 30°N show no coherent patterns while there is some indication of
431 a slight north-eastward self-organization of angular patterns south of 30°N (Fig. 7), which
432 may be associated to the anisotropy observed in the spectra. We do not exhibit the an-
433 gles dependency of the spectral flux due to large confidence intervals.

434 **4 Conclusions and discussion**

435 Using a relatively novel wavelet approach applied to an ensemble of eddy-rich North
436 Atlantic simulations, we claim we can compare local spectra from several spots within
437 the general circulation characterized by vastly different dynamics. Specifically, we com-
438 pare spectra within the recently separated Gulf Stream to those found further downstream,
439 in the inertial recirculation and the gyre interior. The motivation for these comparisons
440 arise from a parameter free definition of ‘eddy’ and interest in clarifying the description
441 of eddies in this heterogeneous field dominated by an ensemble-mean Gulf Stream and
442 relatively quiescent interior. We anticipated that the Gulf Stream would imprint the eddy
443 field with an anisotropic structure, but that the gyre interior would be much simpler and
444 isotropic (Pedlosky et al., 1987). Although an earlier study had warned that the sepa-
445 rated Gulf Stream might not be quasi-geostrophic (QG; Jamet et al., 2020), we nonethe-
446 less expected to see evidences of up-scale energy cascades at scales beyond the deforma-
447 tion radius, and down-scale cascades at shorter length scales, and that spectral slopes
448 would follow QG expectations.

449 Several relatively robust characteristics emerge from our calculations, almost none
450 of which aligned with our hypotheses. As expected, the near separation Gulf Stream was
451 found to be anisotropic at the 95% confidence level. However, beyond this, our analy-
452 sis yielded surprising results. An examination of spectral flux in the near Gulf Stream
453 argued to down scale energy cascades across the spectrum and yielded essentially no ev-
454 idence for an up-scale flux. Consistent with this, with the caveat of large 95% confidence
455 intervals, was a forward flux of enstrophy, although our spectral shape was far steeper
456 than the quasi-geostrophically motivated value of -3 . What was missing was any clear
457 evidence of an upscale cascade. This exceptionally steep (~ -4.2) slope was found across

458 all our spectra, including those in the gyre interior where parameterically QG reason-
459 ing is expected. Another unexpected result was the persistence of anisotropy through-
460 out the interior, with exceptions appearing in the far Gulf Stream and the inertial re-
461 circulation (Fig. 6).

462 Perhaps the most surprising is the gross similarity of the kinetic energy (KE) spec-
463 tral structures throughout the North Atlantic gyre, despite the hugely different dynam-
464 ical regimes in which those spectra are embedded. The local spectra do differ in ampli-
465 tude, with distance from the Gulf Stream associated with a decrease in eddy intensity.
466 This is an expected result. The similarity in spectral slopes we find surprising. We have
467 thus been motivated to compare the gross spectral structures at these locations by nor-
468 malizing the spectra by their locally integrated values over wavenumber (i.e. energy),
469 with the results appearing in Fig. 8. By gross structure, we are referring to the integrated
470 spectra over azimuthal angle prior to normalization. An impression left by this compar-
471 ison is that the spectral shapes are all the same at leading order which, given the zones
472 generating those spectra, is unexpected. The range over which this comparison emerges
473 is that from roughly 300 km to 80 km. At smaller scales, the results diverge, but in view
474 of this result we suggest that the eddy field is occupying a universal shape over a sig-
475 nificant bandwidth. This is a result we had not anticipated but is consistent with Storer
476 et al. (2022) who recently proposed a global universal KE spectrum.

477 While we remain largely unable to offer explanations for our results, we have had
478 some possible success in generalizing the enstrophy inertial-range theory. We can write
479 a potential vorticity (PV) conservation equation for primitive equations, as can be done
480 for a QG system. An unavoidable difference is in the scaling of PV between the two. We
481 argue the dynamically significant difference involves a length scale, which results nat-
482 urally in a steeper slope. To the extent we can assign dynamics to this, the importance
483 of leading order vortex tube stretching is emphasized, and this is a phenomenon easily
484 present in the highly stratified Gulf Stream region. Its relevance there also underscores,
485 and supports, our earlier analysis suggesting QG dynamics do not adequately describe
486 the separated Gulf Stream (Jamet et al., 2020). What we are unable to explain is the
487 appearance of such steep slopes in locations where QG dynamics are expected to dom-
488 inate.

489 In summary, we argue the North Atlantic eddy field is found in an unavoidably in-
 490 homogeneous environment, and exhibits characteristics that we currently have little the-
 491 oretical guidance to interpret. Amongst the most confusing of our results is the incon-
 492 sistent appearance and disappearance of anisotropy in our spectra.

493 The goals of this paper were to apply the wavelet-based technique for estimating
 494 the KE spectra and its spectral flux in realistic simulations where the usual assumptions
 495 of homogeneity and isotropy are clearly suspect. We have demonstrated that the wavelet
 496 method agrees well with the canonical Fourier approach but with the additional strengths
 497 of: i) negating the necessity for the data to be periodic, ii) flexibility in defining the wavenum-
 498 ber resolution via the scaling s , and iii) being able to extract the anisotropy in the flow
 499 through the rotational matrix \mathbf{R} (cf. Uchida, Jamet, et al., 2023). It is also true that the
 500 eddy field is not expected to be stationary, although this is a topic that has not received
 501 any serious attention in this paper. Based on characteristic time scale arguments $\tau =$
 502 \tilde{E}_K/T_K , one might expect the spectra at scales above 100 km to vary on the timescales
 503 of $\sim 10^6$ seconds $\simeq 10$ days looking at Fig. 3a,c. Interestingly, the KE spectra seem
 504 remarkably stable over time whereas its tendency T_K fluctuates rapidly with time (Fig. 4).
 505 While the ensemble technique permits the examination of the time dependence of eddy
 506 spectra, we have only touched upon it here. A more complete examination of the cross-
 507 scale eddy energy transfers is also desirable and possible within the ensemble framework.
 508 And with it, one can examine in more detail the eddy dynamics to address the question
 509 of anisotropic up and down-scale energy transfers. These are amongst the next set of items
 510 we intend to address.

511 A highly related and separate issue involves the examination of potential energy
 512 fluxes. We have here looked solely at the KE spectra. QG theory in its predictions for
 513 up and down scale cascades involves the combined kinetic and potential energies of the
 514 flow. However, in contrast to QG theory, where the resulting total energy is quadratic
 515 and positive definite, primitive equation settings in geopotential coordinates bring no such
 516 guarantees as the eddy dynamic enthalpy is a linear term ($h' \stackrel{\text{def}}{=} h - \langle h \rangle$ following the
 517 notation by Young, 2010); the TWA framework, on the other hand, suggests a (quadratic)
 518 positive-definite total eddy energy when the equation of state for density is linear (cf.
 519 Loose et al., 2022; Uchida, Jamet, et al., 2022, their Appendix A). How to address the
 520 role of potential energy in non-linear cascades and its impact on KE anisotropy is left
 521 for future work.

Open Research

The open-source Fourier and wavelet Python packages are available via Github (Uchida, Rokem, et al., 2021; Uchida & Dewar, 2022). Jupyter notebooks used to conduct the analysis are available via Github (<https://github.com/roxyboy/NA-wavelet-notes/tree/master/Snapshots>; a DOI will be added upon acceptance of the manuscript). The simulation outputs are available on the Florida State University cluster (<http://ocean.fsu.edu/~qjamet/share/data/Uchida2021/>).

Acknowledgments

This study is a contribution to the ‘Assessing the Role of forced and internal Variability for the Ocean and climate Response in a changing climate’ (ARVOR) project supported by the French ‘Les Enveloppes Fluides et l’Environnement’ (LEFE) program. W. K. Dewar is supported through NSF grants OCE-1829856, OCE-1941963 and OCE-2023585, and the French ‘Make Our Planet Great Again’ (MOPGA) program managed by the Agence Nationale de la Recherche under the Programme d’Investissement d’Avenir, reference ANR-18-MPGA-0002. The latter two grants served as the primary support for T. Uchida and partially for Q. Jamet. High-performance computing resources on Cheyenne (doi: 10.5065/D6RX99HX) used for running the NA ensembles were provided by NCAR’s Computational and Information Systems Laboratory, sponsored by NSF, under the university large allocation UFSU0011. We would like to thank Edward Peirce and Kelly Hirai for maintaining the Florida State University cluster on which the data were analyzed.

Appendix A A dynamically consistent buoyancy

For primitive equation models employing a non-linear equation of state (Jackett & McDougall, 1995), the choice of a materially conserved buoyancy variable is non-trivial and has been a subject of debate (e.g. Montgomery, 1937; Jackett & McDougall, 1997; McDougall & Jackett, 2005; de Szoeke & Springer, 2009; Klocker et al., 2009; Tailleux, 2016a, 2016b, 2017, 2021; McDougall et al., 2017; Lang et al., 2020; Stanley et al., 2021). Following Stanley (2019), Stanley and Marshall (2022) and Uchida, Jamet, et al. (2022), we opt for in-situ density anomaly to define the buoyancy $b = -g\delta/\rho_0$ where $\rho_0 = 999.8 \text{ kg m}^{-3}$ is the Boussinesq reference density prescribed in MITgcm. The in-situ density anomaly $\delta (= \rho - \bar{\rho})$ is defined by removing the effect of compressibility while retaining a straight-

552 forward dynamical relation to the horizontal gradients of hydrostatic pressure in Boussi-
 553 nesq fluids; this relation is crucial for dynamical consistency in how buoyancy relates to
 554 momentum. Taking $C_s(z)$ as the maximum sound speed at each depth over the entire
 555 model domain and ensemble, we define $\check{\rho}$ as:

$$556 \quad \check{\rho}(z) = - \int_z^0 \frac{\rho_0 g}{C_s} dz + \rho_0, \quad (\text{A1})$$

557 which reduces to $\check{\rho}|_{z=0} = \rho_0$. δ is subsequently diagnosed as the difference between the
 558 in-situ density and $\check{\rho}$. The interested reader is referred to Uchida, Jamet, et al. (2022)
 559 for further details. While more elaborate techniques may improve the material conser-
 560 vation of δ (and hence b), the relation to the dynamics is non-trivial for other density
 561 variables such as omega, neutral, orthobaric and topological density surfaces (Jackett
 562 & McDougall, 1997; McDougall & Jackett, 2005; Klocker et al., 2009; Stanley, 2019).

563 **Appendix B Spectral budget of the eddy flow**

564 One of the desirable properties of taking the averaging over the ensemble dimen-
 565 sion is that the wavelet transform and averaging operator commute with each other, i.e. $\langle \widetilde{\cdot} \rangle =$
 566 $\widetilde{\langle \cdot \rangle}$, owing to the ensemble dimension being orthogonal to the spatiotemporal dimensions.

567 **B1 Eddy kinetic energy**

568 The ensemble mean kinetic energy (KE; $K^\# = |\langle \mathbf{u} \rangle|^2/2$) equation is given as

$$569 \quad K_t^\# + \langle \mathbf{v} \rangle \cdot \nabla K^\# = -\langle \mathbf{u} \rangle \cdot \nabla_h \langle \phi \rangle - \langle u \rangle \nabla \cdot \langle \mathbf{v}' \mathbf{u}' \rangle - \langle v \rangle \nabla \cdot \langle \mathbf{v}' \mathbf{v}' \rangle + \langle \mathbf{u} \rangle \cdot \langle \mathcal{K} \rangle \quad (\text{B1})$$

571 where $\mathbf{v} = \mathbf{u} + w\mathbf{k}$ is the three-dimensional velocity, and \mathcal{K} is the non-conservative term
 572 consisting of dissipation and contribution from KPP. The total KE, on the other hand,
 573 is

$$574 \quad K_t + \mathbf{v} \cdot \nabla K = -\mathbf{u} \cdot \nabla_h \phi + \mathbf{u} \cdot \mathcal{K}. \quad (\text{B2})$$

575 Now, the total KE can be expanded as

$$576 \quad K = \frac{1}{2} |\langle \mathbf{u} \rangle + \mathbf{u}'|^2 \\ 577 \quad = K^\# + \mathcal{K} + \langle \mathbf{u} \rangle \cdot \mathbf{u}', \quad (\text{B3})$$

579 where $\mathcal{K} = |\mathbf{u}'|^2/2$ so

$$580 \quad \langle \mathbf{v} \cdot \nabla K \rangle = \langle (\langle \mathbf{v} \rangle + \mathbf{v}') \cdot \nabla (K^\# + \mathcal{K} + \langle \mathbf{u} \rangle \cdot \mathbf{u}') \rangle \\ 581 \quad = \langle \mathbf{v} \rangle \cdot \nabla K^\# + \langle \mathbf{v}' \cdot \nabla \mathcal{K} \rangle + \langle \mathbf{v} \rangle \cdot \nabla \langle \mathcal{K} \rangle + \langle \mathbf{v}' \cdot \nabla (\langle \mathbf{u} \rangle \cdot \mathbf{u}') \rangle. \quad (\text{B4})$$

583 Hence, subtracting (B1) from the ensemble mean of (B2) yields

$$584 \quad \langle \mathcal{K} \rangle_t = -\langle \mathbf{u}' \cdot \nabla_{\text{h}} \phi' \rangle - \langle \mathbf{v} \cdot \nabla \mathcal{K} \rangle - \langle \mathbf{v}' \cdot \nabla (\langle \mathbf{u} \cdot \mathbf{u}' \rangle) \rangle + \langle u \rangle \nabla \cdot \langle \mathbf{v}' \mathbf{u}' \rangle + \langle v \rangle \nabla \cdot \langle \mathbf{v}' \mathbf{v}' \rangle + \langle \mathbf{u}' \cdot \mathcal{K}' \rangle, \quad (\text{B5})$$

585 where we see the mean flow and eddies exchanging energy via the term $\langle u \rangle \nabla \cdot \langle \mathbf{v}' \mathbf{u}' \rangle +$
 586 $\langle v \rangle \nabla \cdot \langle \mathbf{v}' \mathbf{v}' \rangle$, which can be interpreted as a eddy forcing onto the mean flow.

587 In order to achieve machine precision in closing the budget using the MITgcm diagnostics
 588 package outputs, we rearrange Equation (B5) as

$$589 \quad \begin{aligned} \langle \mathcal{K} \rangle_t &= -\langle \mathbf{u}' \cdot \nabla_{\text{h}} \phi' \rangle - \langle \mathbf{v} \cdot \nabla \mathcal{K} \rangle - \underbrace{\left(\langle \mathbf{u}' \mathbf{v}' \rangle \cdot \nabla \langle u \rangle + \langle \mathbf{v}' \mathbf{v}' \rangle \cdot \nabla \langle v \rangle + \langle u \rangle \nabla \cdot \langle \mathbf{v}' \mathbf{u}' \rangle + \langle v \rangle \nabla \cdot \langle \mathbf{v}' \mathbf{v}' \rangle \right)}_{= \langle \mathbf{v}' \cdot \nabla (\langle \mathbf{u} \cdot \mathbf{u}' \rangle)} \\ &\quad + \langle u \rangle \nabla \cdot \langle \mathbf{v}' \mathbf{u}' \rangle + \langle v \rangle \nabla \cdot \langle \mathbf{v}' \mathbf{v}' \rangle + \langle \mathbf{u}' \cdot \mathcal{K}' \rangle \\ 590 \quad &= -\langle \mathbf{u}' \cdot \nabla_{\text{h}} \phi' \rangle - \underbrace{\left(\langle \mathbf{u}' (\mathbf{v} \cdot \nabla \mathbf{u}') \rangle + \langle \mathbf{v}' (\mathbf{v} \cdot \nabla \mathbf{v}') \rangle + \langle u \rangle \nabla \cdot \langle \mathbf{v}' \mathbf{u}' \rangle + \langle v \rangle \nabla \cdot \langle \mathbf{v}' \mathbf{v}' \rangle \right)}_{= \langle \mathbf{v} \cdot \nabla \mathcal{K} \rangle + \langle \mathbf{v}' \cdot \nabla (\langle \mathbf{u} \cdot \mathbf{u}' \rangle)} \\ &\quad + \langle u \rangle \nabla \cdot \langle \mathbf{v}' \mathbf{u}' \rangle + \langle v \rangle \nabla \cdot \langle \mathbf{v}' \mathbf{v}' \rangle + \langle \mathbf{u}' \cdot \mathcal{K}' \rangle, \end{aligned}$$

591 where we have also grouped all the divergence terms together as they are neither a source
 592 nor sink of energy and only redistribute it. The spectral budget of eddy KE, therefore,
 593 becomes

$$594 \quad \underbrace{\frac{1}{C_{\Xi}} \langle \tilde{\mathbf{u}}'^* \cdot \tilde{\mathbf{u}}'_t \rangle x_0^2 \kappa}_{T_K} = - \underbrace{\frac{1}{C_{\Xi}} \langle \tilde{\mathbf{u}}'^* \cdot \widetilde{\nabla_{\text{h}}} \phi' \rangle x_0^2 \kappa}_{P_K} \\ 595 \quad - \underbrace{\frac{1}{C_{\Xi}} \left(\langle \tilde{\mathbf{u}}'^* (\widetilde{\mathbf{v}} \cdot \nabla \mathbf{u}') \rangle + \langle \tilde{\mathbf{v}}'^* (\widetilde{\mathbf{v}} \cdot \nabla \mathbf{v}') \rangle + \langle \tilde{u} \rangle^* \nabla \cdot \langle \widetilde{\mathbf{v}' \mathbf{u}'} \rangle + \langle \tilde{v} \rangle^* \nabla \cdot \langle \widetilde{\mathbf{v}' \mathbf{v}'} \rangle \right) x_0^2 \kappa}_{A_K} \\ 596 \quad + \underbrace{\frac{1}{C_{\Xi}} \left(\langle \tilde{u} \rangle^* \nabla \cdot \langle \widetilde{\mathbf{v}' \mathbf{u}'} \rangle + \langle \tilde{v} \rangle^* \nabla \cdot \langle \widetilde{\mathbf{v}' \mathbf{v}'} \rangle \right) x_0^2 \kappa}_{\text{MtE}_K} + \underbrace{\frac{1}{C_{\Xi}} \langle \tilde{\mathbf{u}}'^* \cdot \tilde{\mathcal{K}}' \rangle x_0^2 \kappa}_{\mathcal{K}_K}, \quad (\text{B6}) \\ 597$$

598 (cf. (10)) where MtE_K is the KE exchange between the mean and eddy flow. C_{Ξ} is com-
 599 puted using the `xrft` Python package (Uchida, Rokem, et al., 2021). The horizontal KE
 600 spectral flux often examined by other studies is encapsulated in A_K of (B6).

601 B2 Eddy enstrophy

602 The enstrophy equation is slightly more tractable than the KE equation so we start
 603 off with the mean and eddy Ertel's PV equations neglecting the non-conservative terms

$$604 \quad \langle q \rangle_t + \nabla \cdot (\langle \mathbf{v} \rangle \langle q \rangle) = -\nabla \cdot \langle \mathbf{v}' q' \rangle, \quad (\text{B7})$$

$$605 \quad \langle q'_t \rangle + \nabla \cdot (\langle \mathbf{v} q' \rangle) + \nabla \cdot (\langle \mathbf{v}' \rangle \langle q \rangle) = \nabla \cdot \langle \mathbf{v}' q' \rangle, \quad (\text{B8})$$

607 where the mean flow and eddies exchange PV via the term $\nabla \cdot \langle \mathbf{v}'q' \rangle$. Multiplying each
 608 by $\langle q \rangle$ and q' and taking the ensemble mean gives the mean and eddy enstrophy equa-
 609 tions

$$610 \quad \langle q \rangle \langle q \rangle_t + \langle q \rangle \nabla \cdot (\langle \mathbf{v} \rangle \langle q \rangle) = -\langle q \rangle \nabla \cdot \langle \mathbf{v}'q' \rangle, \quad (\text{B9})$$

$$611 \quad \langle q'q'_t \rangle + \langle q' \nabla \cdot (\mathbf{v}q') \rangle + \underbrace{\langle q' \nabla \cdot (\mathbf{v}' \langle q \rangle) \rangle}_{= \langle \mathbf{v}' \cdot \nabla (\langle q \rangle q') \rangle - \langle q \rangle \nabla \cdot \langle \mathbf{v}'q' \rangle} = 0. \quad (\text{B10})$$

612
 613 In a similar manner to the EKE equation, the eddy enstrophy equation can also be re-
 614 arranged as

$$615 \quad \langle q'q'_t \rangle + \underbrace{\langle q'(\mathbf{v} \cdot \nabla q') \rangle + \langle q \rangle \nabla \cdot \langle \mathbf{v}'q' \rangle}_{= \langle q' \nabla \cdot (\mathbf{v}q') \rangle + \langle \mathbf{v}' \cdot \nabla (\langle q \rangle q') \rangle} = \langle q \rangle \nabla \cdot \langle \mathbf{v}'q' \rangle. \quad (\text{B11})$$

616 Thus, the eddy enstrophy budget in wavelet domain becomes

$$617 \quad \frac{1}{C_{\Xi}} \langle \tilde{q}'^* \tilde{q}'_t \rangle x_0^2 \kappa + \frac{1}{C_{\Xi}} \left[\langle \tilde{q}'^* (\widetilde{\nabla \cdot \mathbf{v}q'})' \rangle + \langle \tilde{q}'^* \widetilde{\nabla \cdot \langle \mathbf{v}'q' \rangle} \right] x_0^2 \kappa = \frac{1}{C_{\Xi}} \langle \tilde{q}'^* \widetilde{\nabla \cdot \langle \mathbf{v}'q' \rangle} \rangle x_0^2 \kappa. \quad (\text{B12})$$

618 We note that the enstrophy budget does not close to machine precision due to the lack
 619 of diagnostics outputs.

620 References

- 621 Ajayi, A., Le Sommer, J., Chassignet, E., Molines, J., Xu, X., Albert, A., & Dewar,
 622 W. (2021). Diagnosing cross-scale kinetic energy exchanges from two sub-
 623 mesoscale permitting ocean models. *Journal of Advances in Modeling Earth*
 624 *Systems*. doi: 10.1029/2019MS001923
- 625 Aoki, K. (2014). A constraint on the thickness-weighted average equation of motion
 626 deduced from energetics. *Journal of Marine Research*, *72*, 355-382. doi: 10
 627 .1357/002224014815469886
- 628 Arbic, B. K., Polzin, K. L., Scott, R. B., Richman, J. G., & Shriver, J. F. (2013).
 629 On eddy viscosity, energy cascades, and the horizontal resolution of gridded
 630 satellite altimeter products. *Journal of Physical Oceanography*, *43*(2), 283-300.
 631 doi: 10.1175/JPO-D-11-0240.1
- 632 Beech, N., Rackow, T., Semmler, T., Danilov, S., Wang, Q., & Jung, T. (2022).
 633 Long-term evolution of ocean eddy activity in a warming world. *Nature cli-*
 634 *mate change*, *12*(10), 910-917. doi: 10.1038/s41558-022-01478-3
- 635 Callies, J., & Ferrari, R. (2013). Interpreting energy and tracer spectra of upper-
 636 ocean turbulence in the submesoscale range (1-200 km). *Journal of Physical*
 637 *Oceanography*, *43*(11), 2456-2474. doi: 10.1175/JPO-D-13-063.1

- 638 Campagne, A., Gallet, B., Moisy, F., & Cortet, P.-P. (2014). Direct and inverse
 639 energy cascades in a forced rotating turbulence experiment. *Physics of Fluids*,
 640 *26*(12), 125112. doi: 10.1063/1.4904957
- 641 Capet, X., McWilliams, J. C., Molemaker, M. J., & Shchepetkin, A. F. (2008).
 642 Mesoscale to submesoscale transition in the california current system. Part I:
 643 Flow structure, eddy flux, and observational tests. *Journal of physical oceanog-*
 644 *raphy*, *38*(1), 29–43. doi: 10.1175/2007JPO3671.1
- 645 Charney, J. G. (1971). Geostrophic turbulence. *Journal of the Atmospheric Sci-*
 646 *ences*, *28*(6), 1087–1095.
- 647 Chassignet, E. P., & Marshall, D. P. (2008). Gulf Stream separation in numerical
 648 ocean models. *Geophysical Monograph Series*, *177*. doi: 10.1029/177GM05
- 649 Chassignet, E. P., Yeager, S. G., Fox-Kemper, B., Bozec, A., Castruccio, F., Dan-
 650 abasoglu, G., ... others (2020). Impact of horizontal resolution on global
 651 ocean–sea ice model simulations based on the experimental protocols of the
 652 Ocean Model Intercomparison Project phase 2 (OMIP-2). *Geoscientific Model*
 653 *Development*, *13*(9), 4595–4637. doi: 10.5194/gmd-13-4595-2020
- 654 Chen, R., & Flierl, G. R. (2015). The contribution of striations to the eddy energy
 655 budget and mixing: Diagnostic frameworks and results in a quasigeostrophic
 656 barotropic system with mean flow. *Journal of Physical Oceanography*, *45*(8),
 657 2095–2113. doi: 10.1175/JPO-D-14-0199.1
- 658 Constantinou, N. C., & Hogg, A. M. (2021). Intrinsic oceanic decadal variability of
 659 upper-ocean heat content. *Journal of Climate*, 1–42. doi: 10.1175/JCLI-D-20
 660 -0962.1
- 661 Daubechies, I. (1992). *Ten lectures on wavelets*. SIAM.
- 662 de Szoeke, R. A., & Springer, S. R. (2009). The materiality and neutrality of neu-
 663 tral density and orthobaric density. *Journal of Physical Oceanography*, *39*(8),
 664 1779–1799. doi: 10.1175/2009JPO4042.1
- 665 Gabor, D. (1946). Theory of communication. Part 1: The analysis of information.
 666 *Journal of the Institution of Electrical Engineers-Part III: Radio and Commu-*
 667 *nication Engineering*, *93*(26), 429–441.
- 668 Gage, K. S., & Nastrom, G. D. (1986). Theoretical interpretation of atmospheric
 669 wavenumber spectra of wind and temperature observed by commercial air-
 670 craft during GASP. *Journal of Atmospheric Sciences*, *43*(7), 729–740. doi:

- 671 10.1175/1520-0469(1986)043<0729:TIOAWS>2.0.CO;2
- 672 Gent, P. R. (2011). The Gent–McWilliams parameterization: 20/20 hindsight.
673 *Ocean Modelling*, *39*(1-2), 2–9. doi: 10.1016/j.ocemod.2010.08.002
- 674 Gent, P. R., & McWilliams, J. C. (1990). Isopycnal mixing in ocean circulation mod-
675 els. *Journal of Physical Oceanography*, *20*(1), 150–155. doi: 10.1175/1520-
676 -0485(1990)020<0150:IMIOCM>2.0.CO;2
- 677 Griffies, S. M., Winton, M., Anderson, W. G., Benson, R., Delworth, T. L., Dufour,
678 C. O., ... others (2015). Impacts on ocean heat from transient mesoscale
679 eddies in a hierarchy of climate models. *Journal of Climate*, *28*(3), 952–977.
680 doi: 10.1175/JCLI-D-14-00353.1
- 681 Guillaumin, A. P., & Zanna, L. (2021). Stochastic-deep learning parameterization
682 of ocean momentum forcing. *Journal of Advances in Modeling Earth Systems*,
683 *13*(9), e2021MS002534. doi: 10.1029/2021MS002534
- 684 Jackett, D. R., & McDougall, T. J. (1995). Minimal adjustment of hydrographic pro-
685 files to achieve static stability. *Journal of Atmospheric and Oceanic Technol-
686 ogy*, *12*, 381-389.
- 687 Jackett, D. R., & McDougall, T. J. (1997). A neutral density variable for the world’s
688 oceans. *Journal of Physical Oceanography*, *27*(2), 237–263. doi: 10.1175/1520-
689 -0485(1997)027<0237:ANDVFT>2.0.CO;2
- 690 Jamet, Q., Deremble, B., Wienders, N., Uchida, T., & Dewar, W. K. (2020). On
691 wind-driven energetics of subtropical gyres. *Journal of Advances in Modeling
692 Earth Systems*, *13*(4), e2020MS002329. doi: 10.1029/2020MS002329
- 693 Jamet, Q., Dewar, W. K., Wienders, N., & Deremble, B. (2019). Spatio-temporal
694 patterns of chaos in the Atlantic Overturning Circulation. *Geophysical Re-
695 search Letters*, doi: 10.1029/2019GL082552.
- 696 Jamet, Q., Leroux, S., Dewar, W. K., Penduff, T., Le Sommer, J., Molines, J.-M., &
697 Gula, J. (2022). Non-local eddy-mean kinetic energy transfers in submesoscale-
698 permitting ensemble simulations. *Journal of Advances in Modeling Earth
699 Systems*. doi: 10.1029/2022MS003057
- 700 Jansen, M. F., Adcroft, A., Khani, S., & Kong, H. (2019). Toward an energetically
701 consistent, resolution aware parameterization of ocean mesoscale eddies. *Jour-
702 nal of Advances in Modeling Earth Systems*, *11*(8), 2844–2860. doi: 10.1029/
703 2019MS001750

- 704 Khatri, H., Griffies, S. M., Uchida, T., Wang, H., & Menemenlis, D. (2021). Role
705 of mixed-layer instabilities in the seasonal evolution of eddy kinetic energy
706 spectra in a global submesoscale permitting simulation. *Geophysical Research*
707 *Letters*, *48*(18), e2021GL094777. doi: 10.1029/2021GL094777
- 708 Khatri, H., Sukhatme, J., Kumar, A., & Verma, M. K. (2018). Surface ocean enstro-
709 phy, kinetic energy fluxes, and spectra from satellite altimetry. *Journal of Geo-*
710 *physical Research: Oceans*, *123*(5), 3875–3892. doi: 10.1029/2017JC013516
- 711 Klocker, A., McDougall, T. J., & Jackett, D. R. (2009). A new method for forming
712 approximately neutral surfaces. *Ocean Science*, *5*(2), 155–172. doi: 10.5194/os-
713 -5-155-2009
- 714 Lang, Y., Stanley, G. J., McDougall, T. J., & Barker, P. M. (2020). A pressure-
715 invariant neutral density variable for the World’s Oceans. *Journal of Physical*
716 *Oceanography*, 1–58. doi: 10.1175/JPO-D-19-0321.1
- 717 Large, W., McWilliams, J., & Doney, S. (1994). Oceanic vertical mixing: A review
718 and a model with a nonlocal boundary layer parameterization. *Reviews of Geo-*
719 *physics*, *32*, 363-403.
- 720 Leroux, S., Penduff, T., Bessières, L., Molines, J.-M., Brankart, J.-M., Sérazin, G.,
721 ... Terray, L. (2018). Intrinsic and atmospherically forced variability of the
722 AMOC: Insights from a large-ensemble ocean hindcast. *Journal of Climate*,
723 *31*(3), 1183–1203. doi: 10.1175/JCLI-D-17-0168.1
- 724 Li, L., Mémin, E., & Tissot, G. (2022). Stochastic parameterization with dynamic
725 mode decomposition. In *Stochastic Transport in Upper Ocean Dynamics*. doi:
726 10.1007/978-3-031-18988-3_11
- 727 Loose, N., Bachman, S., Grooms, I., & Jansen, M. (2022). Diagnosing scale-
728 dependent energy cycles in a high-resolution isopycnal ocean model. *Journal of*
729 *Physical Oceanography*, *53*(1), 157–176. doi: 10.1175/JPO-D-22-0083.1
- 730 Lorenz, E. N. (1963). Deterministic nonperiodic flow. *Journal of atmospheric sci-*
731 *ences*, *20*(2), 130–141. doi: 10.1175/1520-0469(1963)020<0130:DNF>2.0.CO;2
- 732 Marshall, D., Maddison, J., & Berloff, P. (2012). A framework for parameteriz-
733 ing eddy potential vorticity fluxes. *Journal of Physical Oceanography*, *42*, 539-
734 557.
- 735 McDougall, T. J., Groeskamp, S., & Griffies, S. M. (2017). Comment on Tailleux,
736 R. Neutrality versus materiality: A thermodynamic theory of neutral surfaces.

- 737 Fluids 2016, 1, 32. *Fluids*, 2(2), 19. doi: 10.3390/fluids2020019
- 738 McDougall, T. J., & Jackett, D. R. (2005). An assessment of orthobaric density in
739 the global ocean. *Journal of Physical Oceanography*, 35(11), 2054–2075. doi:
740 10.1175/JPO2796.1
- 741 Montgomery, R. (1937). A suggested method for representing gradient flow in isen-
742 tropic surfaces. *Bulletin of the American Meteorological Society*, 18,, 210-212.
743 Retrieved from <http://www.jstor.org/stable/26263980>
- 744 Morlet, J., Arens, G., Fourgeau, E., & Glard, D. (1982). Wave propagation and
745 sampling theory—Part I: Complex signal and scattering in multilayered media.
746 *Geophysics*, 47(2), 203–221. doi: 10.1190/1.1441328
- 747 Pedlosky, J., et al. (1987). *Geophysical fluid dynamics* (Vol. 710). Springer.
- 748 Perrier, V., Philipovitch, T., & Basdevant, C. (1995). Wavelet spectra compared to
749 Fourier spectra. *Journal of mathematical physics*, 36(3), 1506–1519. doi: 10
750 .1063/1.531340
- 751 Poincaré, H. (1890). On the three-body problem and the equations of dynamics.
752 *Acta Math*, 13(1).
- 753 Redi, M. H. (1982). Oceanic isopycnal mixing by coordinate rotation. *Journal*
754 *of Physical Oceanography*, 12(10), 1154–1158. doi: 10.1175/1520-0485(1982)
755 012<1154:OIMBCR>2.0.CO;2
- 756 Rocha, C. B., Chereskin, T. K., Gille, S. T., & Menemenlis, D. (2016). Mesoscale
757 to submesoscale wavenumber spectra in Drake Passage. *Journal of Physical*
758 *Oceanography*, 46(2), 601–620. doi: 10.1175/JPO-D-15-0087.1
- 759 Saba, V. S., Griffies, S. M., Anderson, W. G., Winton, M., Alexander, M. A., Del-
760 worth, T. L., ... others (2016). Enhanced warming of the Northwest At-
761 lantic Ocean under climate change. *Journal of Geophysical Research: Oceans*,
762 121(1), 118–132. doi: 10.1002/2015JC011346
- 763 Scott, R., & Wang, F. (2005). Direct evidence of an oceanic inverse kinetic energy
764 cascade from satellite altimetry. *Journal of Physical Oceanography*, 35, 1650-
765 1666. doi: 10.1175/JPO2771.1
- 766 Sérazin, G., Jaymond, A., Leroux, S., Penduff, T., Bessières, L., Llovel, W., ...
767 Terray, L. (2017). A global probabilistic study of the ocean heat content low-
768 frequency variability: Atmospheric forcing versus oceanic chaos. *Geophysical*
769 *Research Letters*, 44(11), 5580–5589. doi: 10.1002/2017GL073026

- 770 Stainforth, D. A., Allen, M. R., Tredger, E. R., & Smith, L. A. (2007). Confidence,
 771 uncertainty and decision-support relevance in climate predictions. *Philosophical*
 772 *Transactions of the Royal Society A: Mathematical, Physical and Engineering*
 773 *Sciences*, *365*(1857), 2145–2161. doi: 10.1098/rsta.2007.2074
- 774 Stammer, D. (1998). On eddy characteristics, eddy transports, and mean flow prop-
 775 erties. *Journal of Physical Oceanography*, *28*(4), 727–739. doi: 10.1175/1520-
 776 -0485(1998)028<0727:OECETA>2.0.CO;2
- 777 Stammer, D., & Wunsch, C. (1999). Temporal changes in eddy energy of the oceans.
 778 *Deep Sea Research Part II: Topical Studies in Oceanography*, *46*(1-2), 77–108.
 779 doi: 10.1016/S0967-0645(98)00106-4
- 780 Stanley, G. J. (2019). Neutral surface topology. *Ocean Modelling*, *138*, 88–106. doi:
 781 10.1016/j.ocemod.2019.01.008
- 782 Stanley, G. J., & Marshall, D. P. (2022). Why mean potential vorticity cannot
 783 be materially conserved in the eddying Southern Ocean. *Journal of Physical*
 784 *Oceanography*. doi: 10.1175/JPO-D-21-0195.1
- 785 Stanley, G. J., McDougall, T. J., & Barker, P. M. (2021). Algorithmic improve-
 786 ments to finding approximately neutral surfaces. *Journal of Advances in Mod-*
 787 *eling Earth Systems*, *13*(5), e2020MS002436. doi: 10.1029/2020MS002436
- 788 Storer, B. A., Buzzicotti, M., Khatri, H., Griffies, S. M., & Aluie, H. (2022). Global
 789 energy spectrum of the general oceanic circulation. *Nature communications*,
 790 *13*(1), 1–9. doi: s41467-022-33031-3
- 791 Tailleux, R. (2016a). Generalized patched potential density and thermodynamic
 792 neutral density: Two new physically based quasi-neutral density variables
 793 for ocean water masses analyses and circulation studies. *Journal of Physical*
 794 *Oceanography*, *46*(12), 3571–3584. doi: 10.1175/JPO-D-16-0072.1
- 795 Tailleux, R. (2016b). Neutrality versus materiality: A thermodynamic theory of neu-
 796 tral surfaces. *Fluids*, *1*(4), 32. doi: 10.3390/fluids1040032
- 797 Tailleux, R. (2017). Reply to “comment on tailleux, r. neutrality versus materiality:
 798 A thermodynamic theory of neutral surfaces. fluids 2016, 1, 32.”. *Fluids*, *2*(2),
 799 20. doi: 10.3390/fluids2020020
- 800 Tailleux, R. (2021). Spiciness theory revisited, with new views on neutral density,
 801 orthogonality, and passiveness. *Ocean Science*, *17*(1), 203–219. doi: 10.5194/
 802 os-17-203-2021

- 803 Uchida, T., Abernathey, R., & Smith, S. (2017). Seasonality of eddy kinetic energy
 804 in an eddy permitting global climate model. *Ocean Modelling*, *118*, 41–58. doi:
 805 10.1016/j.ocemod.2017.08.006
- 806 Uchida, T., Balwada, D., Abernathey, R., McKinley, G., Smith, S., & Lévy, M.
 807 (2019). The contribution of submesoscale over mesoscale eddy iron transport
 808 in the open Southern Ocean. *Journal of Advances in Modeling Earth Systems*,
 809 *11*(12), 3934–3958. doi: 10.1029/2019MS001805
- 810 Uchida, T., Balwada, D., Jamet, Q., Dewar, W. K., Deremble, B., Penduff, T., &
 811 Le Sommer, J. (2023). Cautionary tales from the mesoscale eddy transport
 812 tensor. *Ocean Modelling*.
- 813 Uchida, T., Deremble, B., Dewar, W. K., & Penduff, T. (2021). Diagnosing the
 814 Eliassen-Palm flux from a quasi-geostrophic double gyre ensemble. In *Earth-*
 815 *cube annual meeting*. Retrieved from [https://earthcube2021.github.io/
 816 ec21_book/notebooks/ec21_uchida_etal/notebooks/TU.05_Diagnosing-the
 817 -Eliassen-Palm-flux-from-a-quasi-geostrophic-double-gyre-ensemble
 818 .html](https://earthcube2021.github.io/ec21_book/notebooks/ec21_uchida_etal/notebooks/TU.05_Diagnosing-the-Eliassen-Palm-flux-from-a-quasi-geostrophic-double-gyre-ensemble.html) doi: 10.5281/zenodo.5496375
- 819 Uchida, T., Deremble, B., & Penduff, T. (2021). The seasonal variability of the
 820 ocean energy cycle from a quasi-geostrophic double gyre ensemble. *Fluids*,
 821 *6*(6), 206. doi: 10.3390/fluids6060206
- 822 Uchida, T., Deremble, B., & Popinet, S. (2022). Deterministic model of the eddy dy-
 823 namics for a midlatitude ocean model. *Journal of Physical Oceanography*. doi:
 824 10.1175/JPO-D-21-0217.1
- 825 Uchida, T., & Dewar, W. K. (2022). *xwavelet: Wavelet transforms for xarray data*
 826 *[Software]*. doi: 10.5281/zenodo.6022738
- 827 Uchida, T., Jamet, Q., Dewar, W. K., Balwada, D., Le Sommer, J., & Penduff, T.
 828 (2022). Diagnosing the thickness-weighted averaged eddy-mean flow interaction
 829 in an eddying North Atlantic ensemble: The Eliassen–Palm flux. *Journal of*
 830 *Advances in Modeling Earth Systems*. doi: 10.1029/2021MS002866
- 831 Uchida, T., Jamet, Q., Poje, A., & Dewar, W. K. (2021). An ensemble-
 832 based eddy and spectral analysis, with application to the Gulf Stream.
 833 *Journal of Advances in Modeling Earth Systems*, e2021MS002692. doi:
 834 10.1029/2021MS002692
- 835 Uchida, T., Jamet, Q., Poje, A., Wienders, N., & Dewar, W. (2023). Wavelet-

- 836 based wavenumber spectral estimate of eddy kinetic energy: Idealized quasi-
 837 geostrophic flow. *Journal of Advances in Modeling Earth Systems*. doi:
 838 10.31223/X5C063
- 839 Uchida, T., Rokem, A., Squire, D., Nicholas, T., Abernathy, R. P., Soler, S.,
 840 ... others (2021). `xrft`: *Fourier transforms for xarray data [Soft-*
 841 *ware]*. Retrieved from <https://xrft.readthedocs.io/en/latest/> doi:
 842 10.5281/zenodo.1402635
- 843 Vallis, G. (2006). *Atmospheric and Oceanic Fluid Dynamics*. Cambridge.
- 844 Vergara, O., Morrow, R., Pujol, I., Dibarboue, G., & Ubelmann, C. (2019). Re-
 845 visited global wave number spectra from recent altimeter observations. *Jour-*
 846 *nal of Geophysical Research: Oceans*, 124(6), 3523–3537. doi: 10.1029/
 847 2018JC014844
- 848 Waterman, S., & Lilly, J. M. (2015). Geometric decomposition of eddy feedbacks in
 849 barotropic systems. *Journal of Physical Oceanography*, 45(4), 1009–1024. doi:
 850 10.1175/JPO-D-14-0177.1
- 851 Wunsch, C. (1981). The Evolution of Physical Oceanography: Scientific Surveys
 852 in Honor of Henry Stommel. In C. Wunsch & B. Warren (Eds.), (p. 342-374).
 853 MIT Press.
- 854 Xu, G., Chang, P., Ramachandran, S., Danabasoglu, G., Yeager, S., Small, J., ...
 855 Wu, L. (2022). Impacts of model horizontal resolution on mean sea-surface
 856 temperature biases in the community earth system model. *Journal of Geophys-*
 857 *ical Research: Oceans*, e2022JC019065. doi: 10.1029/2022JC019065
- 858 Xu, Y., & Fu, L.-L. (2011). Global variability of the wavenumber spectrum of
 859 oceanic mesoscale turbulence. *Journal of Physical Oceanography*, 41(4), 802–
 860 809. doi: <https://doi.org/10.1175/2010JPO4558.1>
- 861 Xu, Y., & Fu, L.-L. (2012). The effects of altimeter instrument noise on the esti-
 862 mation of the wavenumber spectrum of sea surface height. *Journal of Physical*
 863 *Oceanography*, 42(12), 2229–2233. doi: 10.1175/JPO-D-12-0106.1
- 864 Yarom, E., Vardi, Y., & Sharon, E. (2013). Experimental quantification of inverse
 865 energy cascade in deep rotating turbulence. *Physics of Fluids*, 25(8), 085105.
 866 doi: 10.1063/1.4817666
- 867 Young, W. (2010). Dynamic Enthalpy, Conservative Temperature, and the Seawa-
 868 ter Boussinesq Approximation. *Journal of Physical Oceanography*, 40, 394-400.

869 doi: 10.1175/2009JPO4294.1

870 Young, W. (2012). An exact thickness-weighted average formulation of the Boussi-
871 nesq equations. *Journal of Physical Oceanography*, *42*, 692-707. doi: 10.1175/
872 JPO-D-11-0102.1

873 Zhao, M., Ponte, R. M., Penduff, T., Close, S., Llovel, W., & Molines, J.-M. (2021).
874 Imprints of ocean chaotic intrinsic variability on bottom pressure and impli-
875 cations for data and model analyses. *Geophysical Research Letters*, *48*(24),
876 e2021GL096341. doi: 10.1029/2021GL096341

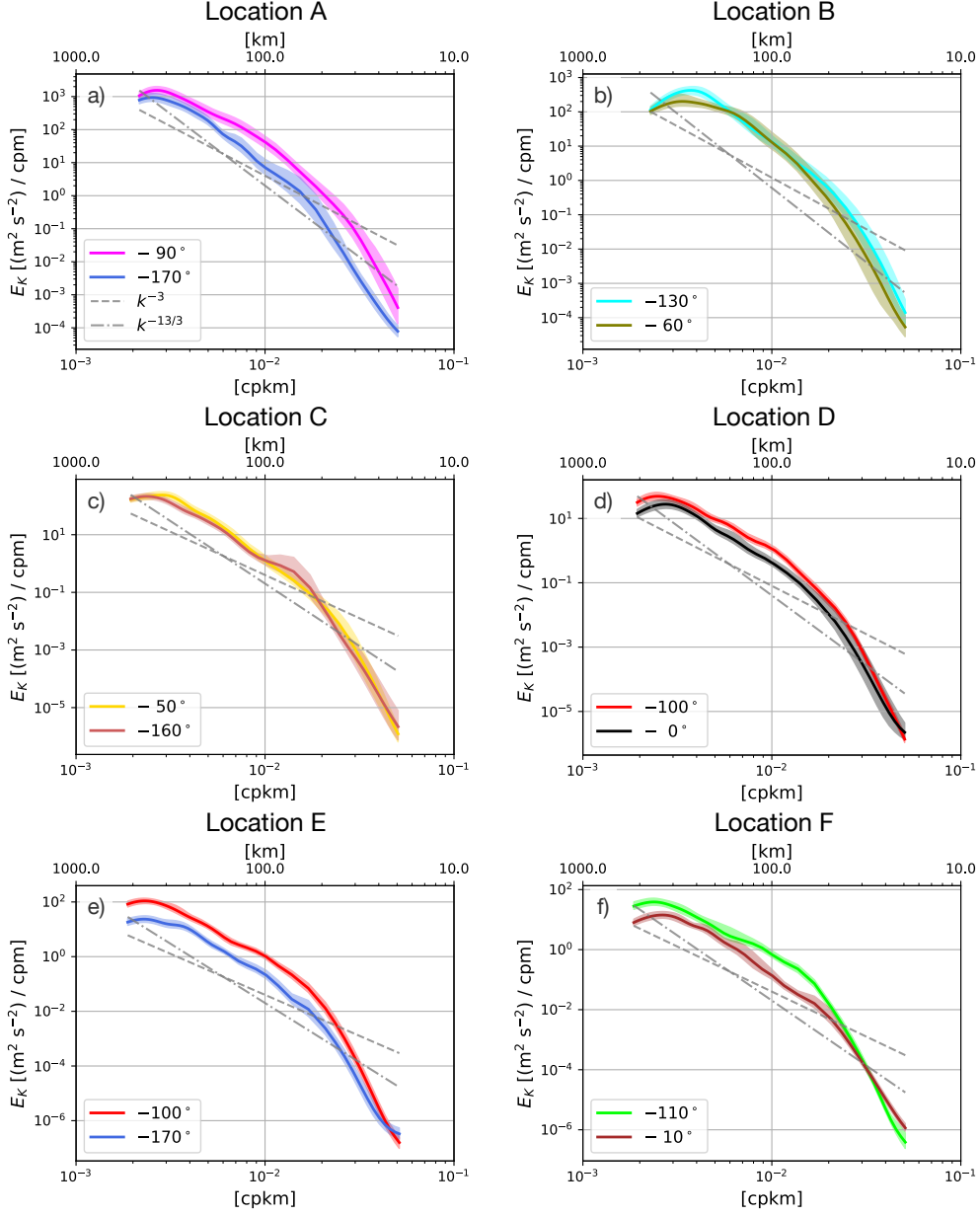


Figure 6. KE spectra $\tilde{E}_K(\phi, k)$ plotted along the orientation of maximum and minimum energy from $z = -452$ m at all six locations (A-F) on January 1, 1967. The angles are color coded. The land cells are not interpolated over and data are not windowed prior to taking the wavelet transforms, differing from Fig. 3a. The 95% bootstrap confidence intervals are shown in colored shadings. Power laws with the slope of -3 and $-13/3$ are indicated with the grey dashed and dotted-dashed curves respectively.

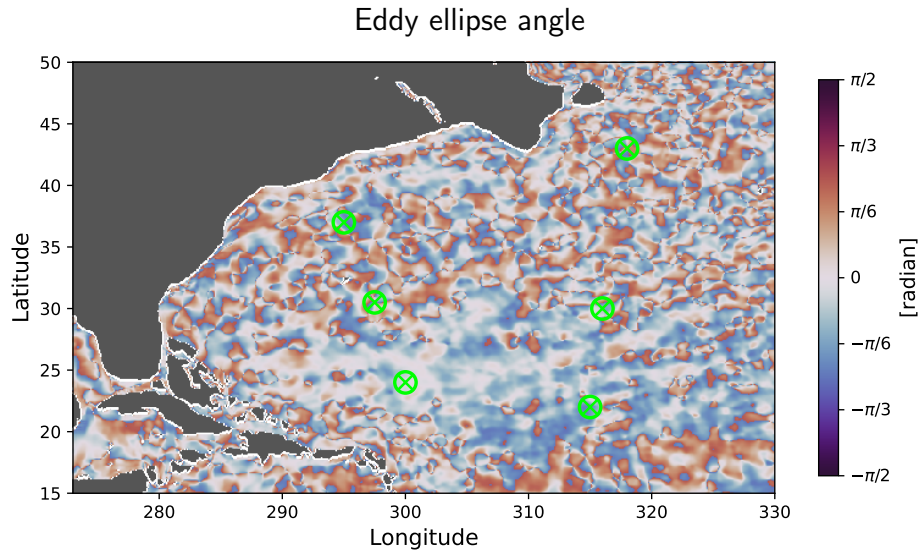


Figure 7. The eddy ellipse angle ϑ at $z = -452$ m on January 1, 1967. The lime-colored \otimes indicate locations A–F.

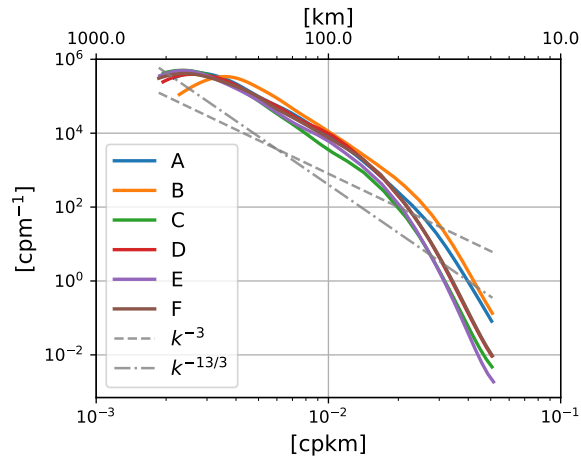


Figure 8. Isotropic KE spectra normalized by their respective energy for locations A–F on January 1, 1967.